RESEARCH ARTICLE

BOPAM: Efficient synthesis of a bright asymmetric bis-boron complex and its dark side

Jianjun Huang,[a] Flip de Jong,[b] Davita Martina Elisa van Raamsdonk,[c] Jonathan Vandenwijngaerden,[b] Akane Inoue,[a] Daniel Escudero,[c] Luc Van Meervelt,[d] Mark Van der Auweraer,[b] and Wim Dehaen*[a]

[a] J. Huang, A. Inoue, Prof. Dr. W. Dehaen
Sustainable Chemistry for Metals and Molecules, Department of Chemistry
KU Leuven
Celestijnenlaan 200F, Leuven 3001(Belgium)
E-mail: wim.dehaen@kuleuven.be

[b] F. de Jong, J. Vandenwijngaerden, Prof. Dr. M. Van der Auweraer
Molecular Imaging and Photonics, Department of Chemistry
KU Leuven
Celestijnenlaan 200F, Leuven 3001(Belgium)
E-mail: mark.vanderauweraer@kuleuven.be

[c] D. van Raamsdonk, Prof. Dr. D. Escudero
Quantum Chemistry and Physical Chemistry, Department of Chemistry
KU Leuven
Celestijnenlaan 200F, Leuven 3001(Belgium)
E-mail: daniel.escudero@kuleuven.be

[d] Prof. Dr. L. Van Meervelt
Biomolecular Architecture, Department of Chemistry
KU Leuven
Celestijnenlaan 200F, Leuven 3001(Belgium)
E-mail: luc.vanmeervelt@kuleuven.be

Abstract:

A new family of unsymmetrical boron chromophores chelated with two BF_2 units, named BOPAM, has been developed via a one-pot three-step reaction starting from commercially available thioamides via (i) conversion to amidrazones, (ii) condensation with pyrrole aldehydes and (iii) boron chelation. This synthetic pathway has been proven to be highly efficient, having a broad substrate tolerance and giving the BOPAM products in high yield. Notably, some of the BOPAM dyes show interesting photophysical properties with fluorescence quantum yields up to 0.98 in toluene. A fine-tuning of their emissive properties has been attained through tailored molecular design strategies guided by in-depth computational investigations. Tailored substitution with electron-donating groups at the BOPAM ring leads to the opening of a non-radiative decay channel involving a dark state and consequently a significant quenching of the fluorescence. The study is complemented by exhaustive steady-state and time-resolved spectroscopic measurements.

Introduction

Nowadays, fluorescent chromophores are increasingly important because of their extensive range of applications.[1–6] For instance, small molecule fluorophores are essential probes for sensing and biological imaging because of the inherent sensitivity of fluorescence techniques.[7–10] More recent applications include opto-electronics such as dye-sensitized solar cells (DSSC)[11–14] and organic light-emitting diodes (OLED).[15–21] The research in these fields benefits from the increased variety of dyes resulting from continuous efforts made in the synthesis and characterization of novel organic luminophores. Organoboron complexes, for instance O,O or N,O-chelated boron diketonates[22,23] and N,N-chelated boron dipyrromethenes (BODIPY)[24], are among the most prominent and well-explored organic fluorophores owing to their easy accessibility, great structural versatility, high photo- and chemical stability as well as narrow absorption and emission bands. Most BODIPY derivatives have relatively small Stokes shifts (400-600 cm^{-1}), which generally leads to the loss of fluorescence in a condensed state due to reabsorption of the emitted light. While their fluorescence range was successfully extended from green to red, BODIPYs emitting in the blue region are less frequently reported.[25]

A significant breakthrough in that regard was the introduction of the symmetric highly fluorescent bis(difluoroboron)1,2-bis((1H-pyrrol-2-yl)methylene)hydrazine (BOPHY) dyes which were reported by Ziegler[26,27] and Hao,[28–30] respectively in 2014. Since then, several functionalization strategies have been developed to optimize BOPHY for different sensing, imaging and photocatalytic applications.[31–33] Likewise, several alternative, unsymmetrical double boron complexed scaffolds have emerged over the past few years. Examples include a pyrrole-N-heteroarene derivate (BOPPY)[34–37] and the pyrrole-acylhydrazone derivatives recently developed independently by our group (BOPAHY) as well as by Hao et al (BOAPY)[38,39] (Figure 1), which exhibit remarkable photophysical properties. We found that careful design is needed to prevent the loss of one of the BF_2 units in polar media, forming the monochelated AIE-active dye BOAHY.[40,41] In this work, we devised a three-step one-pot procedure in which thioamide **1** was initially substituted by hydrazine, followed by acid-catalyzed condensation of the resulting amidrazone **2** with 2-formylpyrrole **3** in ethanol to obtain ligand **4**; Then, deprotonation of the ligand with triethylamine and double boron complexation with boron trifluoride etherate affords the target bis(difluoroboron)pyrrole amidrazone (BOPAM) **5**.

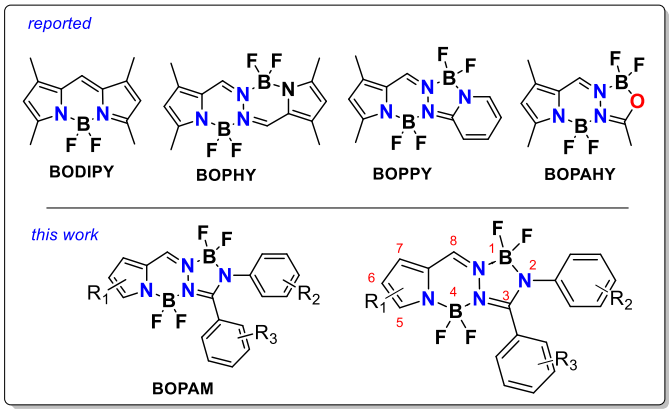

Figure 1. Structure of previously reported BODIPY, BOPHY, BOPPY, BOPAHY chromophores and the novel BOPAM dyes obtained in this work.

More in detail, starting from thioamide **1a** and by heating with hydrazine monohydrate in ethanol for 15 min the amidrazone (N-phenylbenzimidohydrazide) **2a** was formed. After simply evaporating under vacuum to remove the excess hydrazine monohydrate, the residue was redissolved in ethanol and the amidrazone **2a** underwent condensation with 2-formylpyrrole **3a**. The latter step was catalyzed by a few drops of acetic acid. The solvent was again removed in vacuum, and the crude ligand **4a** was dried thoroughly previous to the following boron complexation. Triethylamine was added to deprotonate the ligand and this was subsequently reacted with $BF_3{\cdot}OEt_2$ in dry toluene (Scheme 1). It is important to completely remove all traces of the hydrazine monohydrate in the first step, otherwise BOPHY byproduct is formed, that may be difficult to remove from the BOPAM by chromatographic separation.

Starting from commercially available thioamides or derivatives readily prepared from the reaction of the corresponding amide with Lawesson's reagent, one can easily enlarge the scope of BOPAM derivatives by introducing a wide diversity of side groups onto the BOPAM ring at different positions (see $R_{1\text{-}3}$ in Figure 1). Exploring such a large chemical space and finding tailored molecular design strategies for BOPAMs with optimal photophysical properties with a trial-and-error synthetic approach is time- and resources-consuming. Conversely, even a limited computational pre-screen of this chemical space can help reducing the synthetic efforts. In this contribution, we first explored the excited states and photochemical deactivation pathways of selected BOPAMs using quantum chemical and excited state decay rate theories calculations. The preliminary investigations in **5a** evidenced the existence of a charge transfer excited state (^{1}CT) next to a local excited state (^{1}LE). These ^{1}CT states are basically involved in non-radiative deactivation pathways, and if predominantly populated, this results in quenching the fluorescence[42,43] (i.e., dark-state quenching mechanism). An exploration of the ^{1}CT state revealed that the molecular orbitals participating in the latter state importantly involved the R^2-substituted ring (see below). An EDG (electron donating group) at R^2 may thus, stabilize the ^{1}CT state. To prove this initial hypothesis, we synthesized a new target BOPAM derivative **5i** (see Scheme 2). This allowed us to fully rationalize the photophysical properties of these new BOPAM dyes. In addition, other BOPAM dyes (**5a-5h**, see Figure 2) were synthesized.

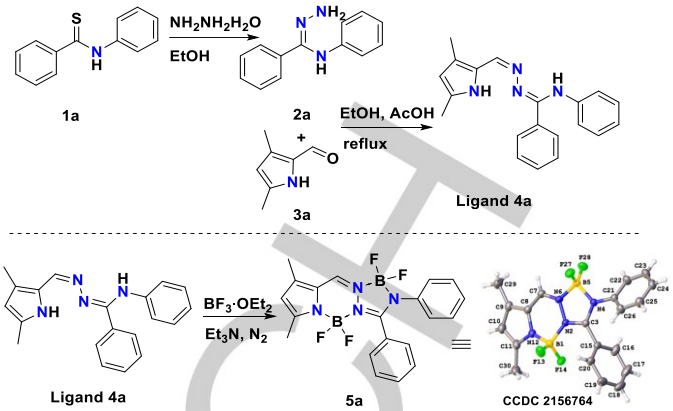

Scheme 1. Synthesis of BOPAM **5a** starting from thio-amide **1a**.

[a] Reaction conditions: **1a** (1.2 mmol), 0.2 mL hydrazine monohydrate, 10 mL EtOH 78 °C; 2-formylpyrrole (1 mmol), 10 mL EtOH and two drops of acetic acid; 25 mL dry toluene , triethylamine (14 mmol, 2 mL) under N_2 in ice-bath keep 15mins, then add $BF_3{\cdot}Et_2O$ (16 mmol) slowly, stirred at room temperature for overnight.

Results and Discussion

The newly synthesized BOPAM derivatives **5a-5h** are shown in Figure 2. The reaction progress was monitored by mass spectrometry. BOPAMs **5a-5h** were synthesized from their corresponding thioamide or pyrrole aldehyde/ketone in good to excellent yields using the same synthetic procedure (see Scheme 1). The best yields are obtained for the substrates with electron-withdrawing groups (EWG) (**5e-5f**). Not surprisingly, the yield of BOPAMs **5g** and **5h** is lower due to the comparatively low reactivity of 2-acetylpyrrole in comparison to the aldehyde analog during the condensation process with amidrazone.

Since thioamides with an EDG like methoxy did not react efficiently with hydrazine, a different synthetic route was explored towards amidrazone **2i** (Scheme 2). Specifically, thionyl chloride was reacted in neat condition with p-benzanisidide **8**. After simple evaporation under vacuum to remove the excess of thionyl chloride, hydrazine in THF was added to the residue, followed by adding 2-formylpyrrole **3a** and similar conversion of the ligand to BOPAM **5i** in 43% overall yield (Scheme 2). All of the BOPAM dyes were stable during the silica column chromatography and characterized by different NMR spectroscopies (^{1}H, ^{13}C, ^{11}B, and ^{19}F) and TOF-HRMS. In the case of BOPAM **5a**, its chemical structure was further confirmed by single-crystal X-ray diffraction analysis (see Scheme 1). In comparison to BOPAHYs, the boron NMR spectrum exhibits two triplet signals instead of one triplet and another singlet. Through ^{13}C NMR spectrum analysis, the presence of a fluorine atom at the 4-position (as shown in Figure 1) of the BF_2 unit resulted in the splitting of the nearest carbon atom on ring substituent R_3, observed as a triplet signal.

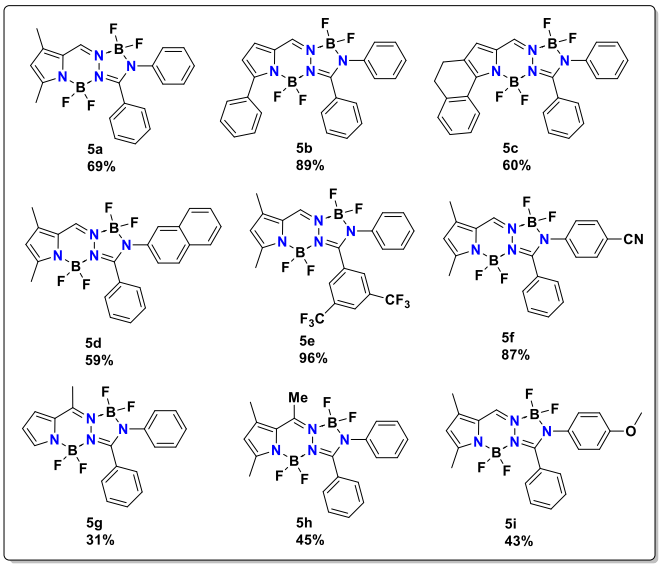

Figure 2. Scope of the substrate towards BOPAM **5a-5i**

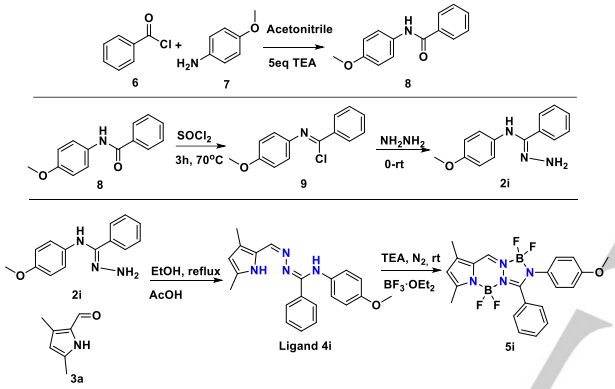

Scheme 2. Synthetic route of BOPAM **5i**.

All synthesized BOPAMs were fully characterized using UV-Vis and fluorescence spectroscopy in both solution and solid state (i.e., powder). Table 1 summarizes the key data and the fitting parameters for the more complex decays can be found in Table S16. Firstly, the photophysical properties of **5a-5i** in solution will be discussed.

Comparing the parent compound **5a** to the similar sized methyl substituted BOPAHY[38,39] (λ_{abs} = 383 nm, λ_{em} = 396 nm in toluene), the new BOPAM dye possesses slightly redshifted bands. These redshifts can readily be explained by the replacement of oxygen by a more electron donating nitrogen and/or by the extra delocalization over the 3-phenyl ring, which is visible in the electron density difference plots presented in **Table S12** for the bright transitions of **5a**. These plots also indicate that the 2-phenyl ring is less involved in the bright excited state. For all BOPAMs the absorption and emission spectra (with the exception of **5e** and **5i**) blueshift going from the polarizable solvent toluene to the polar but less polarizable solvent acetonitrile, which indicates the lack of a significant ground-state and excited-state dipole moments.[44–46] The extinction coefficients for **5a** (41700 $M^{-1}cm^{-1}$), **5c** (52500 $M^{-1}cm^{-1}$) and **5i** (43400 $M^{-1}cm^{-1}$) are close to those reported for triazole-substituted BOPAHY or BOPPY.[34,47] The higher value for **5c** can be readily explained from its extended conjugation.

Table 1. Selected photophysical data for BOPAM **5a-5i** in toluene, MeCN and solid state (powder) at room temperature. The excitation wavelengths for the powders is given in Table S16. **5b** and **5c** showed different emission spectra, depending on the crystallisation method, see discussion. [a]Extinction coefficient ε = 41700 $M^{-1}cm^{-1}$. [b]ε = 52500 $M^{-1}cm^{-1}$. [c]ε = 43400 $M^{-1}cm^{-1}$.

Solvent	Dye	λ_{abs} (nm)	λ_{em} (nm)	$\bar{\nu}_{abs}$-$\bar{\nu}_{em}$ (cm^{-1})	$FWHM_{em}$ (cm^{-1})	Energy eV	Φ_F	τ_F (ns)
Toluene	**5a**	402[a]	461	3180	3720	2.89	0.41	1.12
	5b	413	464	2660	3090	2.82	0.84	2.29
	5c	450[b]	479	1350	2680	2.67	0.98	2.63
	5d	400	471	3770	3800	2.90	0.05	0.17
	5e	401	499	4900	4180	2.84	0.38	1.48
	5f	398	473	3980	3850	2.89	0.84	2.34
	5g	372	441	4210	3900	3.08	0.06	0.17
	5h	389	457	3830	3910	3.00	0.47	1.27
	5i	399[c]	476	4050	4420	2.92	0.01	See SI
MeCN	**5a**	391	455	3600	4090	3.00	0.20	0.62
	5b	398	470	3850	3310	2.87	0.79	2.20
	5c	439	475	1730	2000	2.72	0.96	3.06
	5d	392	475	4460	4490	2.96	0.02	See SI
	5e	394	515	5960	4690	2.88	0.18	1.04
	5f	394	471	4150	4370	2.97	0.46	1.72
	5g	363	436	4610	4450	3.15	0.02	0.08
	5h	383	456	4180	4330	3.06	0.14	0.52
	5i	393	547	7160	8090	3.02 (LE) 2.27 (CT)	<0.01	See SI
Solid state	**5a**	431	494	2950	2440	-	0.36	See SI
	5b(o)	414	594	7320	3540	-	0.45	
	5c(y)	450	594	5390	3580	-	0.45	
	5d	432	500	3130	3700	-	0.12	
	5e	416	484	3410	3270	-	0.09	
	5f	434	506	3270	3320	-	0.38	
	5g	394	477	4460	4710	-	0.16	
	5h	412	487	3690	4520	-	0.22	
	5i	429	487	2780	3500	-	0.13	

For all compounds except **5d** and **5i** the fluorescence decay could be fitted to a single exponential. For **5a** decay times of 1.12 ns in toluene and 0.62 ns in acetonitrile (Table 1) were found. Combining these decay times with the fluorescence quantum yield allowed us to calculate a fluorescent rate constant of $3.66x10^8$ s^{-1} and $3.23x10^8$ s^{-1} in toluene and acetonitrile; respectively (see Table S19). The slightly smaller value in acetonitrile can be related to the smaller refractive index of this solvent, considering that the Einstein coefficient for spontaneous emission is proportional with the cube of the refractive index. The values of k_f are close to the computed one (Table S14, *cf. infra*) and of the same order of magnitude as those obtained for BODIPY or cyanine dyes.[44,48] This indicates a completely allowed transition from the ^{1}LE state. The lower fluorescence quantum yield in acetonitrile compared to toluene is due to a more than twofold increase of the rate constant for radiationless decay (k_{nr}). The multi-exponential decay of **5d** and **5i** points to competing deactivation channels and will be discussed in a later section.

Comparing excitation energies on basis of absorption or emission maxima is quite difficult for the BOPAM derivatives as these maxima sometimes correspond to 0-0 transitions (mainly for the spectra showing residual fine structure), while for the structureless spectra they are more likely to correspond to 0-1 transitions. The latter can be seen in the spectra where the 0-0 transition is only observable as a small shoulder on the red side of the absorption or the blue side of the emission spectra (Figure 3 and Figures S7-S10). In order to avoid the ambiguity in the comparisons between the computed and the experimental results (see below), we also report the crossing point between the normalized absorption and emission spectra. The crossing point is directly comparable to the adiabatic energy difference between S_0 and ^{1}LE corrected by their corresponding zero-point vibrational energies (i.e., ΔE_{00}) (see Tables 1, S10).

Substitution of the 5-methyl group by a 5-phenyl group decreases ΔE_{00} from 2.89 eV in **5a** to 2.82 eV in **5b** and fixing this phenyl group in the plane of the five membered ring by an ethylene bridge decreases the ΔE_{00} value further to 2.67 eV in **5c**. This decrease of the ΔE_{00} value is also reflected in the observed red shift of the absorption and emission spectra and it can be attributed to an extension of the conjugated system over the phenyl ring. The delocalization is also clearly visible in the computed electron density difference (EDD) plot of S_1 for **5c** (Figure 3 and Table S12). Introducing the phenyl substituent in the 5-position also significantly increases the photoluminescence quantum yield (PLQY) in toluene from 0.41 for **5a** to 0.84 for **5b**. A further rigidification of the conjugated system with an ethylene bridge in **5c** leads to a further increase of the PLQY up to 0.98 in toluene and 0.96 in MeCN. From the data presented in Table S18 it is clear that the improved PLQY values are due to the significant decrease of the non-radiative decay rate. Interestingly, the restricted rotation of the 5-phenyl leads to a more pronounced vibrational fine structure both in the absorption and emission spectra and to a much smaller full width of half maximum of the emission ($FWHM_{em}$) for **5c** than for any other BOPAMs (see Table 1). The latter indicates a smaller electron-vibrational coupling reducing the Franck Condon factor for internal conversion. While this reduced electron-vibrational coupling of **5c** compared to **5b** can be attributed to blocking the rotation of the phenyl group by the ethylene bridge it is less clear why replacing the methyl by the phenyl group reduces the electron-vibrational coupling in **5b** compared to **5a**. Actually, an opposite behavior was observed for a BODIPY derivative where replacing a methyl group by a phenyl group in the 8-position led to a strong reduction of the PLQY.[49] When rationalizing the different behavior of **5c** versus **5a**, it is instructive to have a look at two similar structures from the BOPPY family which were recently reported[36,37] (structures in Scheme S1, SI part 5). Compound **S1** misses the 5- and 7-methyl with respect to **5a** and features a fused quinoline at position 2 and 3. Compared to **5a** its PLQY is enhanced dramatically to unity (in DCM). This already reveals the importance of the 2-substituent. Molecule **S2** has a bridged structure reminiscent of **5c** and additionally a 2,3-fused 6-chloro-2-pyridine, resulting in a large redshift in the emission, different vibrational fine structure and a decrease of the PLQY value to 0.24 (toluene).

Looking at **5h**, we can conclude that the introduction of an 8-methyl substituent has little impact on the photophysical properties. The small blueshift can be related to the introduction of an electron donating methyl group on a position where upon excitation the electron density is increased (Figure 3, Table S12). Removing the 5- and 6-methyl groups in **5g** results in a strong blueshift. Furthermore, an order of magnitude decrease in the PLQY value is observed in **5g** as compared to the one in **5h**. This can be attributed to a very large value of the rate constant for radiationless decay, k_{nr}, which even exceeds 10^{10} s^{-1} in MeCN (see Table S18). This large difference in k_{nr} is difficult to explain as a similar $FWHM_{em}$ value indicates a similar electron-vibrational coupling and resulting Franck-Condon factors for internal conversion in **5g** and **5h**.

For **5e** the effect of the electron withdrawing 3-[3,5-bis(trifluoromethyl)phenyl] substituent can be evaluated. While the absorption characteristics and the PLQY value is not changed with respect to those of **5a**, the emission is redshifted about 1700 cm^{-1} in toluene and about 2400 cm^{-1} in MeCN. Also the ΔE_{00} value decreases by 400 cm^{-1} in toluene and 1000 cm^{-1} in MeCN as compared to those of **5a**. As visualized in the EDD plot of S_1 for **5a** (see Figure 3 and Table S12) there is an increased electron density on the 3-phenyl ring in S_1. Thus, the excited state gets more stabilized than the ground state by the electron withdrawing CF_3 and this leads to a decrease of the excitation energy. One should also note that with exception of **5i**, which shows dual emission (*cf. infra*) in MeCN, **5e** has the largest $FWHM_{em}$ value and it shows a red shifted emission in MeCN compared to the one observed in toluene. This suggests a net permanent dipole moment in the excited state by shifting electron density to the CF_3-subsituted 3-phenyl ring. It is interesting to note that **5e** features by far the lowest radiative rate constant in both solvents even when the $\bar{\nu}_{em}^3$ dependence of k_f is considered.

Going from **5f** over **5a** to **5d** and finally to **5i** only small differences in absorption and emission wavelengths are noted (with exception of the maximum of **5i** emission in MeCN (*cf. infra*)). This correlates with the observation in the EDD plots related to S_1 of the BOPAMs, which can predominantly be described as a local excited (^{1}LE) state (Table S12). Notably, the 2-phenyl ring is less involved in the conjugation than the 3-phenyl ring, and it shows no involvement in S_1.

We note that the PLQY values are systematically lower in MeCN than in toluene. Additionally, they systematically decrease when going from **5f** to **5a**, **5d** and **5i** with increasing electron donating or decreasing electron withdrawing character of the aromatic substituent in the 2 position (see Table 1). While in toluene **5d** is characterized by a value of k_{nr} which exceeds by an order of magnitude that of the other compounds (except **5g** and probably **5i**), its decay becomes bi-exponential in MeCN suggesting the formation of a second excited-state species. The short decay time corresponds to the time to establish an equilibrium between the ^{1}LE and this second excited state species while the long decay

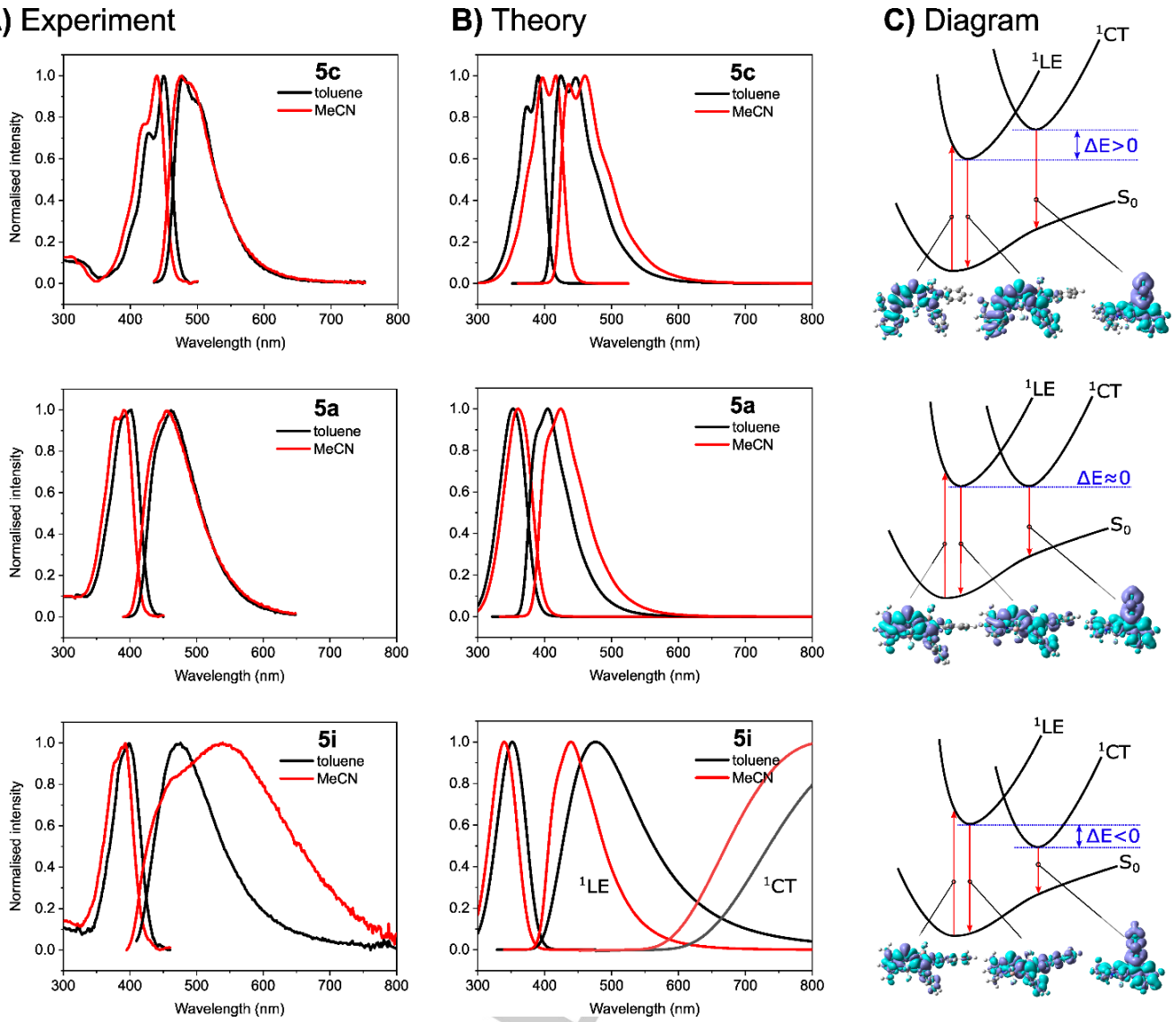

Figure 3. Photophysical behaviour of selected BOPAM dyes (**5c**, **5a** and **5i**). (A) Normalised UV-Vis absorption spectra and emission spectra in toluene (black) and MeCN (red). (B) Corresponding computed vibronically resolved spectra for the LE state. For **5i** also the computed emission spectra for the CT state are given. (C) Schematic representation of the singlet electronic states of interest. Electron density difference (EDD) plots are shown for the possible electronic transitions from and to the ground state (isovalue 0.0004). The purple and blue lobes indicate increase and decrease of the electron density, respectively. From left to right: the S_0 to LE transition (ground state geometry), the LE to S_0 transition (geometry of the LE state) and the CT to S_0 transition (geometry of the CT state).

time is the inverse of a weighted average of the decay rates (Table S16).[50,51]

For **5d** in MeCN, the ratio of the pre-exponential factors of the fast and slow decaying components of the decay suggests that the equilibrium between the ^{1}LE state and the second excited state species is nearly completely shifted to the latter. The short decay time will then be very close to the inverse of the rate of the interconversion from the ^{1}LE state to the other one and reflects the fluorescence lifetime of the ^{1}LE state. Combining this with the observed fluorescence quantum yield yields a value of k_f of 3.3×10^8 s^{-1} which is close to what would be expected for an ^{1}LE state. This agrees with the observation that the emission spectrum of **5d** in MeCN is very similar to that in toluene. The involvement of a second excited state becomes clearer for **5i** where the fluorescence decay is bi- and tri-exponential in respectively toluene and MeCN, while in MeCN the spectral features clearly show the occurrence of dual emission. Besides a shoulder at 470 nm, related to the ^{1}LE state, a broad maximum is observed at 547 nm (see Figure 3), related to the second excited state species which is possibly a ^{1}CT state (*cf. infra*). As for **5i** the short decay time is close to time resolution of the experimental set-up, a quantitative interpretation of the multi-exponential decays of **5i** is difficult. The nature of both states and their potential decay channels will be elucidated below with the help of quantum chemical calculations.

Quantum chemical calculations were performed on **5a**, **5b**, **5c**, **5f** and **5i** to elucidate the nature of the involved excited states and the corresponding excited state decay pathways (see details in the Experimental Section).

Apart from the properties of the low lying ^{1}LE state, we also report on the vertical absorption, emission energy and oscillator strength of the lowest excited state of CT character, ^{1}CT (see Table S8-

S10). These results suggest that the observed first UV-Vis absorption and emission bands (except perhaps for **5i** in MeCN) are due to the ^{1}LE state. For the TD-DFT results, the excitation energies are overestimated by 0.3-0.7 eV while the emission energies are overestimated by 0.1-0.5 eV. These errors are well documented for cyanine dyes[52] and related BODIPY dyes.[49] Aiming at a higher accuracy we also performed ADC(2) calculations (see discussion in the SI). In acetonitrile, the computed ADC(2) emission energies are overall in closer agreement with the experiment (deviations amounting up to ca. 0.3 eV), except for **5i**. The computed ΔE_{00} values are in good agreement with the crossing point between the absorption and emission spectra (deviations amounting up to ca. 0.2 eV), see Tables 2 and S10. In Figure 3 and Figure S4 and S5, the computed vibronically-resolved absorption and emission spectra are displayed along with their experimental counterparts. Overall, the features of the computed spectra match reasonably well with the experimental spectra, but the computed spectra are significantly blueshifted, which could be expected from the discrepancy between the calculated and experimental absorption and emission maxima (Tables S8 and S9). Note for instance that the vibrational fine structure observed for **5c** is recovered by our calculations. The computed k_f values are also in good agreement with the experimental values (compare computed and experimental values in Tables S14 and S18). For **5i** in MeCN the calculated ^{1}LE emission energy is close to the energy of the short wavelength shoulder in the emission spectrum (470 nm). Therefore, this shoulder can be attributed to emission from the ^{1}LE state. Comparing the experimental maximum at 547 nm (2.27 eV) and the calculated emission maximum of the ^{1}CT state at 778 nm (1.59 eV) (Table S9), we however obtain a discrepancy of 0.7 eV. Also for the other studied compounds (**5a**, **5c**, **5f**) the calculated energy of the ^{1}CT emission (Table S9) is much below than that of the ^{1}LE state but dual emission was not observed for the latter compounds, only for **5i** (see discussion below). In Figure 4 the geometrical features of the optimized structures of the ^{1}LE and ^{1}CT states along with that of the optimized mimimum energy crossing point (MECP) connecting both states are shown. The optimized geometry of the ^{1}LE state is characterized by a mostly flat disposition of the BOPAM core and the R_2-substituted ring. Conversely, in the optimized geometry of the ^{1}CT state, the R_2-substituted ring is tilted out of the plane by pyramidalization of the nitrogen atom. This is clearly reflected in the dihedral angle highlighted in green in Figure 4, which changes from 195.5 degrees in the ^{1}LE geometry to 99.6 degrees in the ^{1}CT geometry. This perpendicular orientation of the 2-aryl substituent in the ^{1}CT state is a general phenomenon for all compounds for which the properties of this state were calculated (see Table S12). The corresponding EDD plots also show that in this ^{1}CT state charge density is shifted from this substituent to the rest of the molecule as the transition $^1\text{CT} \rightarrow S_0$ increases the charge density in this moiety. The direction of the charge transfer means that increasing electron donating character of the 2-substuent will stabilize this ^{1}CT state. This involvement of this ^{1}CT state in the radiationless decay of the ^{1}LE state is compatible with the observed increase of k_{nr} when the electron donating character of the substituent is increased from **5f** over **5a**, **5d** to **5i**. In a similar way it explains why k_{nr} is increased when the solvent is changed from the apolar toluene to the polar MeCN which will stabilize the ^{1}CT state versus the ^{1}LE state.

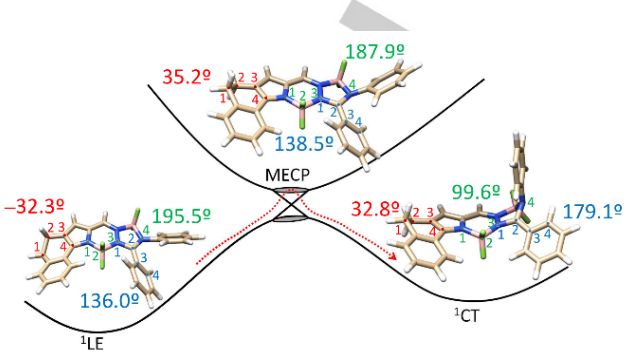

Figure 4. ^{1}LE→^{1}CT deactivation pathway for **5c**. The main geometrical parameters of the optimized geometries of the ^{1}LE, ^{1}CT and MECP in the gas phase are highlighted.

Starting from this CT-hypothesis we systematically explored the possible ^{1}LE→^{1}CT interconversion for selected BOPAM (i.e., **5a**, **5b**, **5c**, **5i** and **5f**), trying to relate it to the experimentally observed efficiency of the non-radiative decay. The ^{1}LE→^{1}CT interconversion is schematically presented in Figure 3C for **5c**, **5a** and **5i**, as representatives of a high, medium and very low fluorescence quantum yield. In Table 2 the computed adiabatic energy differences between the ^{1}LE and ^{1}CT states are collected. The computed ^{1}LE and ^{1}CT energy levels for **5i** (3.28 and 3.27 eV, respectively in MeCN) vs the ones for **5a** (3.33 and 3.54 eV) or those of **5f** (3.27 and 3.70 eV) clearly show a different energetic ordering of the ^{1}LE and ^{1}CT states for **5i**, being the ^{1}CT state adiabatically lower in energy than the ^{1}LE state. We recall that **5i** shows a quasi-complete quenching of the ^{1}LE fluorescence. On the other hand, the series **5c**, **5b**, **5a** shows that raising the energy of the ^{1}LE state, while keeping that of the ^{1}CT state more or less constant (see Table 2, results in gas phase and toluene), leads to a similar decrease of the barrier and a corresponding increase in k_{nr}. The involvement of the ^{1}CT state in the radiationless decay of the ^{1}LE state now allows to explain why replacing the methyl (**5a**) by a phenyl (**5b**) reduces the rate of internal conversion in contrast to what was observed for 8-substitution of BODIPYs.[49] The next step in our investigation of the ^{1}LE→^{1}CT deactivation pathway involved the optimization of the MECP for **5c**, see e.g., in Figure 4. While the geometry of the relaxed ^{1}CT state differs strongly from that of the ^{1}LE state (*cf. supra*), the geometry of the optimized MECP or minimum energy conical intersection resembles more the geometry of the ^{1}LE state than that of the ^{1}CT. We note that the MECP geometry is characterized by a slight pyramidalization of the nitrogen atom connected to the R_2-substituted ring. The MECP could successfully be optimized for **5a**, **5b** and **5c** (see the associated barriers in Table S13). For **5b** and **5c** the MECP is located high in energy above the ^{1}LE minimum, which will lead to a negligible ^{1}LE→^{1}CT interconversion (see Table S13). Thus, at RT, the thermal population of the ^{1}CT state from ^{1}LE is not expected to compete efficiently with other decay processes from the ^{1}LE state, such as fluorescence or intersystem crossing. Consequently, the ^{1}CT state will not be significantly populated, which agrees well with a value of k_{nr} which is at least an order of magnitude smaller in **5b** and **5c**. In the case

of **5a** the barrier is significantly smaller, and thus an Arrhenius rate on the order of 10^7 is derived. Therefore, in **5a** the population of the ^{1}CT state might compete with other decay processes from ^{1}LE, which in turn could explain the lower quantum yield and larger k_{nr} with respect to e.g. **5b**. Note that small inaccuracies in the computed barriers translate exponentially into the rates, so obtaining accurate excited state decay rates is challenging.[53] For **5i**, **5f** all attempts to optimize a MECP geometry were unsuccessful, however, the energy differences between the ^{1}LE and ^{1}CT states collected in Table 2 provide an indirect hint on the plausibility of a fast and efficient ^{1}LE→^{1}CT interconversion. Two extreme situations, i.e., **5c** and **5i**, can be compared further. For **5c**, the ^{1}CT state is always higher in energy than the ^{1}LE state, regardless of the solvent (see Table 2). This is in agreement with the largest computed activation barrier for **5c**. Oppositely, **5i** possess the smallest difference between the ^{1}LE and ^{1}CT states (3.28 vs. 3.27 eV, respectively in MeCN, see Table 2), and thus, the ^{1}LE→^{1}CT interconversion proceeds in a barrierless manner in the case of **5i**. Accordingly, an almost complete quenching of the fluorescence is experimentally observed.

Table 2. Adiabatic TDA TD-DFT energies (eV) of ^{1}LE and ^{1}CT states. Energies given in gas phase, toluene, and acetonitrile for 5a; 5b; 5c; 5f and 5i. ΔE (eV) is given as $E_{CT} - E_{LE}$.

System	Gas Phase			toluene			MeCN		
	LE (eV)	CT (eV)	ΔE (eV)	LE (eV)	CT (eV)	ΔE (eV)	LE (eV)	CT (eV)	ΔE (eV)
5a	3.59	3.31	-0.28	3.45	3.43	-0.02	3.33	3.54	0.21
5b	3.44	3.27	-0.17	3.3	3.41	0.11	3.18	3.55	0.37
5c	3.30	3.28	0.28	3.15	3.3	0.15	3.23	3.51	0.28
5f	3.54	3.45	-0.09	3.4	3.59	0.19	3.27	3.70	0.43
5i		3.04		3.35	3.16	-0.19	3.28	3.27	-0.01

While the model involving the ^{1}CT state can be used for quantitative and qualitative arguments to explain the dependence of k_{nr} on the molecular structure in a consequent way, the relation between the red shifted emission of **5i** in MeCN and the ^{1}CT state is less straightforward. Both the calculated maximum (table S9) and the calculated emission spectrum (Fig 3 bottom) of this ^{1}CT state are red shifted by 0.67 eV or more than 200 nm compared to the observed long wavelength band in MeCN. Considering that for the ^{1}LE state the calculated energy is always somewhat higher than the experimental one, this gap becomes even larger. A possible hypothesis for this 'intermediate emission' would be a partial CT-state intermediate between the ^{1}LE and the fully relaxed ^{1}CT state, as was previously observed for e.g. conjugates of indolo[3-2-b]carbazole and boron-dipyrromethene or diketopyrrolopyrrole.[54] Such interpretation is also compatible with the observed fluorescence decays. At 550 nm, where in this framework nearly all emission is due to the unrelaxed CT state, the analysis of the fluorescence decays shows that the component with a 31 ps decay time contributes for more than 90 % to the stationary emission. This suggests that this decay time, rather than representing the time for equilibration between the ^{1}LE and ^{1}CT state, as concluded earlier for **5d** (*cf. supra*) is a common decay time for the ^{1}LE and unrelaxed ^{1}CT state towards a dark fully relaxed ^{1}CT state. Equilibration between the originally populated ^{1}LE and unrelaxed ^{1}CT state occurs then on a time scale beyond the time resolution of the set-up used. In this conceptual framework, the slower decaying components are probably due to small amounts of impurities which explains why their relative amplitude decreases rather than increases at longer wavelengths.[50,51]

In order to further explore the photophysics of **5i**, nanosecond transient absorption experiments were performed. No long-lived (> 10 ns) excited state could be detected. This indicates that if the ^{1}CT state is formed it relaxes rapidly to S_0 and that no long living triplet states are formed with a significant quantum yield. A fast decay of the ^{1}CT state to the ground state makes sense considering the large geometry difference which will lead to a strong electron phonon coupling and a large Franck-Condon factor for internal conversion. The computed small emission energies from the ^{1}CT state, along with the relatively small computed ^{1}CT→^{3}LE ISC rates (see Table S14), fully align with the experimental pieces of evidence.

Also the solids of BOPAM feature emission spectra that, although being strongly red shifted compared to solution (Figures 4 and S11-19), often show some trace of vibrational fine structure.. Because of the large fluorescence quantum yields of up to 0.45, it was essential to exclude fluorescent photons for the diffuse reflectance measurements, see experimental details in the SI. This accounts for the sometimes poor signal-to-noise ratio of these spectra.

For **5f** to **5h** the emission spectra in the solid state resemble those in toluene but their maxima are red shifted by 1350 to 1730 cm^{-1} while the absorption spectra are shifted by between 1470 and 2100 cm^{-1}. For **5d** and **5e** similar results are obtained, although the maxima of the emission spectra are only shifted by 400 to 1230 cm^{-1}. By comparing the different compounds, we can explain this by noting that while for **5f** to **5h** the emission maxima in the solid state correspond to the 0→1 transition those for **5d** and **5e** correspond to the 0→0 transition. On the other hand, in toluene all maxima correspond to the 0→1 transition. For **5i** a similar shift (1750 cm^{-1}) of the maximum of the absorption spectrum is observed although the maximum of the emission spectrum only shifted for 480 cm^{-1} compared to toluene. This red shift observed for the absorption and emission spectra of **5d** to **5i** can be attributed to interaction between neighboring chromophores.[55–59] The size of the shift is close to what is observed for exciton interaction in aggregates of cyanine dyes, *i.e.* other chromophores with a large oscillator strengh and corresponding transition dipole for the $S_0 \rightarrow S_1$ transition.[60–63] The similar red shift

observed for absorption and emission spectra furthermore suggests the formation of J-type rather than H-type aggregates.[58]

The excitation spectra of **5d**, **5e**, **5f** and **5i** resemble the absorption spectra but often have a more pronounced long wavelength maximum. While the main maximum of the excitation spectra of **5g** and **5h** corresponds to that of the absorption spectrum, they also show a second red shifted maximum/shoulder at 460 nm, 475 nm for respectively **5g** and **5h**. Considering the small Stokes shift of only 520 to 840 cm^{-1} between this second maximum and the emission maximum, which is much smaller than the Stokes shifts observed in solution (Table 1), it is unlikely that this shoulder is related to the species giving the main emission. This discrepancy suggests the presence of more than one emitting species which becomes even clearer when considering the wavelength dependence of the fluorescence decays (Table S18). Upon increasing the emission wavelength the amplitude of the component(s) with the shortest decay time(s) decreases (and sometimes even becomes negative) while that of the component(s) with longer decay time(s) increases. The long wavelength band in the excitation spectrum is in this framework related to a species with stronger J-type intermolecular interactions, leading to a stronger red shift of absorption and emission spectra.

At all wavelengths, the fluorescence decays of **5d** to **5i** could be analyzed as a sum of three or four exponentials. One must realize that also non-exponential decays related to energy transfer to traps in solids[64] can be analyzed as sum of exponentials[65] or that decays with more than three exponentially decaying components can be analyzed as a sum of three exponentials. Hence, one can probably not directly link the individual components of the decays and the corresponding decay times to species present in the solid dye. Still, it was possible to link the decay times over several emission wavelengths and study the wavelength dependence of the amplitudes of the different exponential components, showing a strong dependence with those of the fastest decaying component even becoming negative at long wavelengths. In spite of the limitations on the accuracy of the analysis of the decays mentioned above, this allows us to conclude that some species emitting at long wavelength are populated by energy transfer from species absorbing and emitting at shorter wavelengths. When the average decay time $\langle\tau\rangle$ time was calculated as

$$\langle\tau\rangle = \frac{\sum A_i \tau_i}{\sum A_i}$$

Values between 0.51 and 2.26 ns (Table S19) were obtained for **5d** to **5i** using decays determined close to the emission maximum (Table S18). Combine the values of $\langle\tau\rangle$ with the fluorescence quantum yields (Table 1) values between 1.23×10^8 s^{-1} and 3.56×10^8 s^{-1} were obtained for k_f. for **5d** to **5i**. These values are somewhat smaller than the solution values. However one should consider that the presence of different emitting species and the non-exponential and wavelength dependent decays severely impact the accuracy with which k_f can be determined. Furthermore, the red shift of the emission compared to solution will for an identical transition dipole lead to a decrease of k_f which is proportional with the cube of the wavenumber of the emission. The recovered values of k_f are compatible with J-type rather than with H-type aggregates, where the radiative transition from the lowest exciton level is forbidden.[55–57]

The solid-state emission spectrum of **5a** consists of a very clear vibrational progression around starting at 494 nm and a high-energy shoulder at 464 nm. The maximum is redshifted by 1450 cm^{-1} versus a solution of **5a** in toluene, which resembles the shift obtained for **5d** where the maximum of the emission spectrum in toluene also corresponds to the 0→1 transition while it corresponds for both compounds to the 0→0 transition in the solid state. The absorption maximum at 431 nm is redshifted by 1680 cm^{-1} versus toluene, this shift is again resembling the shifts obtained for **5d** to **5i**. One should note that the absorption spectrum extends to nearly 500 nm, with a small shoulder around 475 nm. In the excitation spectrum of the emission at 460 and 500 nm the longest wavelength band is at 437 nm which, considering the poor signal to noise of the absorption spectra, probably corresponds with the absorption band. For the emission at 530 and 570 nm the excitation spectrum also contains a second band with maximum around 479 nm, corresponding with the red tail of the absorption band. This species absorbing and emitting at longer wavelengths is, in analogy to **5g** to **5i,** attributed to species with stronger intramolecular interactions. The presence of different emitting species is also revealed by the wavelength dependence of the components of the fluorescence decays, as shown in Table S17. This table clearly shows that the emission at 450-460 nm, corresponding to the blue shoulder of the emission spectrum must be attributed to another species as that responsible for the emission at the maximum (494 nm). Hence, the short wavelength shoulder of the emission spectrum does not belong to the vibrational progression of the main emitting species which continues to resemble that in toluene in spite of the intermolecular interactions leading to a significant red shift of absorption, emission and excitation spectra. At long wavelengths the amplitude of the component with the shortest decay time is negative. This suggest that, besides by direct excitation at long wavelengths (479 nm), the species emitting at longer wavelength can also be excited by energy transfer from the species emitting at shorter wavelengths. Combining the average fluorescence decay time of 2.53 ns obtained for the emission at 500 nm with the fluorescence quantum yield of 0.36 yielded a value of 1.42×10^8 s^{-1} for k_f. This large value of k_f , combined with the similar red shift of both absorption or excitation and emission spectra indicate that the species responsible for the most important component of the emission is a J-type rather than a H-type aggregate.

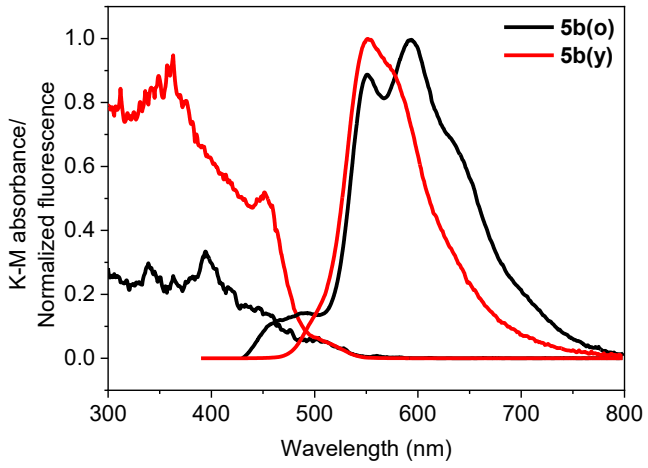

Figure 5. Kubelka-Munk converted diffuse reflectance and normalized fluorescence spectra of the powders **5b(o)** and **5b(y)**.

For **5b** and **5c**, an additional complication is presented by the different spectra obtained for two different purification methods (Sample **5b(o)** was crystalized from pure DCM and **5b(y)** was crystalized from pentane/DCM v/v=1:1 mixture), these datasets are empirically labelled orange (o) and yellow (y). Comparing **5b(o)** and **5b(y)** (Figure 5), we note that the band at 551 nm is present in both spectra, but going from (y) to (o) two additional band systems appear, a less intense blue shifted system around 490 nm and an intense red shifted system with a maximum at 594 nm, contributing to further broadening of the main emission band from ca. 2650 to 3550 cm^{-1}. While the blue shifted shoulder of **5b(o)** is close to the maximum of the solution spectra, the band at 551 nm is shifted to a larger extent (i.e. 3500 cm^{-1}) compared to the solution spectra than was observed for **5a** and **5d** to **5i**. From the excitation spectra we can infer that the blue shifted bands in **5b(o)** can be excited directly at around 410 nm (close to the maximum of the solution spectra), while excitation in the red edge of the absorption spectrum yields the fluorescence at 551 nm and 594 nm. Excitation spectra taken at 555, 600 and 645 nm are remarkably similar, suggesting the latter two bands are populated in the same way. Notwithstanding the caution applied earlier when interpreting multi-exponential fits to complex decay data, here it might be possible to attribute physical meaning to the amplitudes and lifetimes fitted to the fluorescence decay of **5b(y)**, as in the main fluorescence band, the 2.71 ns component has a contribution of around 90%, with a small contribution of a longer component, which, after comparison with the values retrieved for **5b(o),** might be assigned to small amounts of the species giving rise to the additional redshifted band at 594 nm in **5b(o)**. Additionally, a very distinct growing in of the fluorescence was observed, suggesting population of the excited state through energy transfer from the possibly monomeric species discernible as a shoulder in the blue edge of the spectrum of **5b(y)**. Continuing with this hypothesis we can make similar assignments for the more complicated case of **5b(o)**, where the decay curve at 490 nm shows a fast, probably non-exponential decay, which again can be explained by energy transfer to the 551 and 594 nm bands. The 551 nm band, when probed at 555 nm reveals a small growing in and two positive amplitude lifetimes, 1.45 ns and 2.44 ns, while going to 600 and 645 nm we also probe the red shifted band at 594 nm explaining the longer lifetime 4.06 ns and again a distinct rise time of the fluorescence decay. For **5c** the band around 590 nm remains the most important, but both the blue shifted and the red shifted bands are already present in **5c(y)**. This further complicates the analysis, but the similar behavior, including the prominent rise times and the increased weight of the longer lifetimes at longer wavelengths obtained from both the **5c** samples, points to the same mechanism as proposed for **5b**, namely excitation of the higher energy state first (possibly the monomer) and subsequent excitation transfer to the lower-lying dimer or aggregate states.

Conclusion

In conclusion, we have successfully prepared a series of novel bisboron complexes called BOPAM via a relatively simple one-pot synthetic pathway from accessible starting materials. The presented strategy provides a facile protocol for the efficient and modular construction of novel boron complexes which are featuring a great functional group tolerance, and operational simplicity.

To understand and rationalize the subtleties on the photophysical properties of the BOPAMs, which are fine-tuned by ligand substitutions, in-depth steady-state and time-resolved spectroscopic studies as well as computational investigations have been performed. Importantly, the use of EDG at R^2 leads to an almost quantitative quenching of fluorescence, which has unambiguously been rationalized to the presence of a low-lying ^{1}CT dark-state.

While in solution the highest QY achieved was 0.98, also in solid a respectable QY of 0.45 could be obtained. We show that the powder as synthesized is not phase pure, but that emission occurs from very well-defined species. Although the intermolecular interactions between neighboring molecules lead to J-type rather than H-type aggregation, the absence of superradiance characterized by a value of k_f exceeding several times that of monomers in solution suggest the absence of long range order of the aggregated chromophores.

Compared to BODIPY, the emission is blueshifted and the quantum yields in aggregated state are much higher. The performance is closer to BOPHY and BOPPY dyes, but the different scaffold proposed in this work allows for different substitution patterns to control its photophysical properties. An advantage over the BOPAHY reported earlier is its increased stability. Further research will be undertaken towards the post-functionalization of the dye. Possible applications as solid-state luminescent materials, labelling reagents and fluorescent sensors will be communicated in due course.

Acknowledgements

J. Huang appreciates the financial support from the China Scholarship Council (CSC) for providing a doctoral scholarship. D. E. and W. D acknowledge FWO in the framework of a bilateral FWO-NAFOSTED program (Project number: G0E5321N) for financial support. FdJ thanks the Research Foundation–Flanders (FWO) for FWO-SB fellowship 1SC4719N. FWO is also thanked

for the support of a Scientific Research Community (Project nr W000620).

Conflict of interest

The authors declare no conflict of interest.

Keywords: BOPAM • photophysical propeties• theoretical calculations.

[1] L. Yuan, W. Lin, K. Zheng, L. He, W. Huang, *Chem Soc Rev* **2013**, *42*, 622–661.

[2] J. Zhao, K. Xu, W. Yang, Z. Wang, F. Zhong, *Chem. Soc. Rev.* **2015**, *44*, 8904–8939.

[3] W. Guan, W. Zhou, J. Lu, C. Lu, *Chem. Soc. Rev.* **2015**, *44*, 6981–7009.

[4] A. Bessette, G. S. Hanan, *Chem Soc Rev* **2014**, *43*, 3342–3405.

[5] Y.-J. Shiu, Y.-C. Cheng, W.-L. Tsai, C.-C. Wu, C.-T. Chao, C.-W. Lu, Y. Chi, Y.-T. Chen, S.-H. Liu, P.-T. Chou, *Angew. Chem. Int. Ed.* **2016**, *55*, 3017–3021.

[6] N. Boens, V. Leen, W. Dehaen, *Chem. Soc. Rev.* **2012**, *41*, 1130–1172.

[7] J. X. J. Zhang, K. Hoshino, *Molecular Sensors and Nanodevices: Principles, Designs and Applications in Biomedical Engineering*, Academic Press, **2018**.

[8] Y. Zhou, J. Yoon, *Chem Soc Rev* **2012**, *41*, 52–67.

[9] M. H. Lee, J. S. Kim, J. L. Sessler, *Chem. Soc. Rev.* **2015**, *44*, 4185–4191.

[10] D. Cao, Z. Liu, P. Verwilst, S. Koo, P. Jangjili, J. S. Kim, W. Lin, *Chem. Rev.* **2019**, *119*, 10403–10519.

[11] A. Carella, F. Borbone, R. Centore, *Front. Chem.* **2018**, *6,* 481.

[12] K. Sharma, V. Sharma, S. S. Sharma, *Nanoscale Res. Lett.* **2018**, *13*, 381.

[13] J. Gong, J. Liang, K. Sumathy, *Renew. Sustain. Energy Rev.* **2012**, *16*, 5848–5860.

[14] A. Hagfeldt, G. Boschloo, L. Sun, L. Kloo, H. Pettersson, *Chem. Rev.* **2010**, *110*, 6595–6663.

[15] C.-T. Chen, *Chem. Mater.* **2004**, *16*, 4389–4400.

[16] T. Tsutsui, N. Takada, *Jpn. J. Appl. Phys.* **2013**, *52*, 110001.

[17] P. Li, H. Chan, S.-L. Lai, M. Ng, M.-Y. Chan, V. W.-W. Yam, *Angew. Chem. Int. Ed.* **2019**, *58*, 9088–9094.

[18] A. Salehi, X. Fu, D.-H. Shin, F. So, *Adv. Funct. Mater.* **2019**, *29*, 1808803.

[19] J.-H. Lee, C.-H. Chen, P.-H. Lee, H.-Y. Lin, M. Leung, T.-L. Chiu, C.-F. Lin, *J. Mater. Chem. C* **2019**, *7*, 5874–5888.

[20] S.-J. Zou, Y. Shen, F.-M. Xie, J.-D. Chen, Y.-Q. Li, J.-X. Tang, *Mater. Chem. Front.* **2020**, *4*, 788–820.

[21] W. Zhang, F. Zhang, R. Tang, Y. Fu, X. Wang, X. Zhuang, G. He, X. Feng, *Org. Lett.* **2016**, *18*, 3618–3621.

[22] P. Sen, L. S. Mpeta, J. Mack, T. Nyokong, *J. Lumin.* **2020**, *224*, 117262.

[23] J. Huang, L. Bourda, S. Tusupbayev, B. Li, Y. Wang, Z.-G. Hong, W. Zhang, A. Makhmet, A. A. Peshkov, S. Kashtanov, M. Krasavin, K. Van Hecke, O. P. Pereshivko, V. A. Peshkov, *Dyes Pigments* **2023**, *217*, 111374.

[24] R. Yoshii, A. Hirose, K. Tanaka, Y. Chujo, *J. Am. Chem. Soc.* **2014**, *136*, 18131–18139.

[25] M. Bacalum, L. Wang, S. Boodts, P. Yuan, V. Leen, N. Smisdom, E. Fron, S. Knippenberg, G. Fabre, P. Trouillas, D. Beljonne, W. Dehaen, N. Boens, M. Ameloot, *Langmuir* **2016**, *32*, 3495–3505.

[26] I.-S. Tamgho, A. Hasheminasab, J. T. Engle, V. N. Nemykin, C. J. Ziegler, *J. Am. Chem. Soc.* **2014**, *136*, 5623–5626.

[27] H. M. Rhoda, K. Chanawanno, A. J. King, Y. V. Zatsikha, C. J. Ziegler, V. N. Nemykin, *Chem. – Eur. J.* **2015**, *21*, 18043–18046.

[28] J. Wang, Q. Wu, C. Yu, Y. Wei, X. Mu, E. Hao, L. Jiao, *J. Org. Chem.* **2016**, *81*, 11316–11323.

[29] X. Lv, T. Li, Q. Wu, C. Yu, L. Jiao, E. Hao, *J. Org. Chem.* **2018**, *83*, 1134–1145.

[30] J. Wang, X. Fang, X. Guo, Q. Wu, Q. Gong, C. Yu, E. Hao, L. Jiao, *Org. Lett.* **2021**, *23*, 4796–4801.

[31] S. Boodts, J. Hofkens, W. Dehaen, *Dyes Pigments* **2017**, *142*, 249–254.

[32] S. Boodts, E. Fron, J. Hofkens, W. Dehaen, *Coord. Chem. Rev.* **2018**, *371*, 1–10.

[33] A. N. Bismillah, I. Aprahamian, *Chem. Soc. Rev.* **2021**, *50*, 5631–5649.

[34] C. Yu, Z. Huang, X. Wang, W. Miao, Q. Wu, W.-Y. Wong, E. Hao, Y. Xiao, L. Jiao, *Org. Lett.* **2018**, *20*, 4462–4466.

[35] X. Jiang, S. Yue, K. Chen, Z. Shao, C. Li, Y. Su, J. Zhao, *Chin. Chem. Lett.* **2019**, *30*, 2271–2273.

[36] L. Cui, H. Shinjo, T. Ichiki, K. Deyama, T. Harada, K. Ishibashi, T. Ehara, K. Miyata, K. Onda, Y. Hisaeda, T. Ono, *Angew. Chem. Int. Ed.* **2022**, *61*, e202204358.

[37] C. Yu, Y. Sun, X. Fang, J. Li, Q. Wu, W. Bu, X. Guo, H. Wang, L. Jiao, E. Hao, *Inorg. Chem.* **2022**, *61*, 16718–16729.

[38] C. Yu, X. Fang, Q. Wu, L. Jiao, L. Sun, Z. Li, P.-K. So, W.-Y. Wong, E. Hao, *Org. Lett.* **2020**, *22*, 4588–4592.

[39] S. Pookkandam Parambil, F. de Jong, K. Veys, J. Huang, S. P. Veettil, D. Verhaeghe, L. Van Meervelt, D. Escudero, M. Van der Auweraer, W. Dehaen, *Chem. Commun.* **2020**, *56*, 5791–5794.

[40] C. Yu, E. Hao, X. Fang, Q. Wu, L. Wang, J. Li, L. Xu, L. Jiao, W.-Y. Wong, *J. Mater. Chem. C* **2019**, *7*, 3269–3277.

[41] F. de Jong, D. Verhaeghe, K. Veys, J. Huang, S. P. Parambil, W. Dehaen, D. Escudero, E. Fron, M. Van der Auweraer, *Dyes Pigments* **2022**, *206*, 110662.

[42] D. Escudero, *Acc. Chem. Res.* **2016**, *49*, 1816–1824.

[43] Y. Yan, A. A. Sukhanov, M. H. E. Bousquet, Q. Guan, J. Zhao, V. K. Voronkova, D. Escudero, A. Barbon, Y. Xing, G. G. Gurzadyan, D. Jacquemin, *J. Phys. Chem. B* **2021**, *125*, 6280–6295.

[44] W. Qin, M. Baruah, M. Van Der Auweraer, F. C. De Schryver, N. Boens, *J. Phys. Chem. A* **2005**, *109*, 7371–7384.

[45] E. von Lippert, *Z. Für Elektrochem. Berichte Bunsenges. Für Phys. Chem.* **1957**, *61*, 962–975.
[46] N. Mataga, Y. Kaifu, M. Koizumi, *Bull. Chem. Soc. Jpn.* **1956**, *29*, 465–470.
[47] T. Horsten, F. de Jong, D. Theunissen, M. Van der Auweraer, W. Dehaen, *J. Org. Chem.* **2021**, *86*, 13774–13782.
[48] N. Vranken, S. Jordens, G. De Belder, M. Lor, E. Rousseau, G. Schweitzer, S. Toppet, M. Van Der Auweraer, F. C. De Schryver, *J. Phys. Chem. A* **2001**, *105*, 10196–10203.
[49] L. Jiao, C. Yu, J. Wang, E. A. Briggs, N. A. Besley, D. Robinson, M. J. Ruedas-Rama, A. Orte, L. Crovetto, E. M. Talavera, J. M. Alvarez-Pez, M. Van der Auweraer, N. Boens, *RSC Adv.* **2015**, *5*, 89375–89388.
[50] D. V. O'Connor, W. R. Ware, *J. Am. Chem. Soc.* **1976**, *98*, 4706–4711.
[51] Man Him Hui, W. R. Ware, *J. Am. Chem. Soc.* **1976**, *98*, 4718–4727.
[52] B. Le Guennic, D. Jacquemin, *Acc. Chem. Res.* **2015**, *48*, 530–537.
[53] K. Veys, D. Escudero, *Acc. Chem. Res.* **2022**, *55*, 2698–2707.
[54] A. Khetubol, S. Van Snick, M. L. Clark, E. Fron, E. Coutino-Gonzalez, A. Cloet, K. Kennes, Y. Firdaus, M. Vlasselaer, V. Leen, W. Dehaen, M. Van der Auweraer, *Photochem. Photobiol.* **2015**, *91*, 637–653.
[55] M. Kasha, *Radiat. Res.* **1963**, *20*, 55–70.
[56] E. G. McRae, M. Kasha, in *Phys. Process. Radiat. Biol.*, Elsevier, **1964**, pp. 23–42.
[57] A. P. Deshmukh, N. Geue, N. C. Bradbury, T. L. Atallah, C. Chuang, M. Pengshung, J. Cao, E. M. Sletten, D. Neuhauser, J. R. Caram, *Chem. Phys. Rev.* **2022**, *3*, 021401.
[58] A.-C. Nellissen, R. Steeno, J. B. F. Vandenwijngaerden, S. De Feyter, S. F. L. Mertens, M. Van der Auweraer, *Dyes Pigments* **2023**, *208*, 110790.
[59] T. Forster, *Naturwissenschaften* **1946**, *33*, 166–175.
[60] I. G. Scheblykin, O. P. Varnavsky, W. Verbouwe, S. De Backer, M. Van der Auweraer, A. G. Vitukhnovsky, *Chem. Phys. Lett.* **1998**, *282*, 250–256.
[61] M. Van der Auweraer, I. Scheblykin, *Chem. Phys.* **2002**, *275*, 285–306.
[62] M. Van Der Auweraer, G. Biesmans, F.-C. De Schryver, *Chem. Phys.* **1988**, *119*, 355–375.
[63] G. Biesmans, M. Van der Auweraer, F. C. De Schryver, *Langmuir* **1990**, *6*, 277–285.
[64] G. Zumofen, A. Blumen, *Chem. Phys. Lett.* **1982**, *88*, 63–67.
[65] M. Van der Auweraer, P. Ballet, F. C. De Schryver, A. Kowalczyk, *Chem. Phys.* **1994**, *187*, 399–416.

WILEY-VCH

Entry for the Table of Contents

WILEY-VCH